Generation and Validation of Broadband Synthetic *P* Waves in Semistochastic Models of Large Earthquakes

Dara E. Goldberg*[1] and Diego Melgar[1]

ABSTRACT

We present an approach for generating stochastic scenario rupture models and semistochastic broadband seismic waveforms that include validated *P* waves, an important feature for application to early warning systems testing. There are few observations of large magnitude earthquakes available for development and refinement of early warning procedures; thus, simulated data are a valuable supplement. We demonstrate the advantage of using the Karhunen–Loève expansion method for generating stochastic scenario rupture models, as it allows the user to build in desired spatial qualities, such as a slip inversion, as a mean background slip model. For waveform computation, we employ a deterministic approach at low frequencies (< 1 Hz) and a semistochastic approach at high frequencies (> 1 Hz). Our approach follows Graves and Pitarka (2010) and extends to model *P* waves. We present the first validation of semistochastic broadband *P* waves, comparing our waveforms against observations of the 2014 M_w 8.1 Iquique, Chile, earthquake in the time domain and across frequencies of interest. We then consider the *P* waves in greater detail, using a set of synthetic waveforms generated for scenario ruptures in the Cascadia subduction zone. We confirm that the time-dependent synthetic *P*-wave amplitude growth is consistent with previous analyses and demonstrate how the data could be used to simulate earthquake early warning procedures.

KEY POINTS

- We use the Karhunen–Loève expansion to generate stochastic rupture models using a background slip distribution.
- We generate semistochastic broadband seismic waveforms and include *P* waves for application to early warning.
- We perform a formal validation of semistochastic *P* waves in both the time and frequency domains.

INTRODUCTION

The development of robust earthquake and tsunami hazard response, including ground-motion prediction for early warning systems, requires diverse datasets for testing and validation of operational methods (Allen and Melgar, 2019). Observational datasets are especially scarce for large magnitude earthquakes; thus, the performance of rapid response systems for the greatest magnitude events is not well understood. The M_w 9.0 Tohoku-Oki earthquake is currently the only earthquake of great magnitude observed in the nearfield with modern seismic and geodetic technology, and thus is often used as a proxy for tectonic environments in which similar M_w 9.0 earthquakes are expected, like the Cascadia Subduction Zone (CSZ), for which no instrumental data for damaging megathrust events exist. Although using this single event to test the performance of earthquake early warning (EEW) algorithms is valuable, it may not be entirely informative of an algorithm's performance for future earthquakes of similar magnitude.

Scenario ruptures and physically realistic synthetic waveforms are a necessary substitute for observations to facilitate validation and refinement of existing operational practices. One approach to generation of scenario ruptures is to select a correlation function (typically von Karman) and relevant parameters to model the synthetic fault-slip distributions. Using the von Karman correlation function, for example, the user defines a Hurst exponent and correlation lengths in the strike and dip directions to control the slip roughness and the dominant size of slip asperities (Mai and Beroza, 2002).

1. Department of Earth Sciences, University of Oregon, Eugene, Oregon, U.S.A.
*Corresponding author: dgoldber@uoregon.edu

Cite this article as Goldberg, D. E., and D. Melgar (2020). Generation and Validation of Broadband Synthetic *P* Waves in Semistochastic Models of Large Earthquakes, *Bull. Seismol. Soc. Am.* **XX**, 1–14, doi: 10.1785/0120200049

From this statistical description of slip, random realizations of rupture patterns are achieved by one of two main methodologies: (1) in the wavenumber domain, assigning the correlation function amplitude spectrum and a random phase, before inverse Fourier transformation to the spatial domain (e.g., Graves and Pitarka, 2010); or (2) directly in the spatial domain, using the Karhunen–Loève (K-L) expansion (LeVeque *et al.*, 2016). Both methods can be used to produce a target slip model, such as one with spatial features similar to a historical event. Using the wavenumber domain method, this involves creating many iterations and selecting the random number seed that produces a visually compatible model. As we will show here, the K-L expansion approach is convenient, because it allows the user to build in desired spatial qualities, such as using a predefined mean static slip pattern from a known event as a base model. For both of these approaches, the static slip pattern is converted to a kinematic model based upon assumptions of the earthquake rupture speed and duration, as well as the shape of the of local slip rate (the rise time and slip rate function) (e.g., Melgar *et al.*, 2016). Adding random variability to static and kinematic parameters creates realistic slip patterns with complexities typical of real earthquakes (Graves and Pitarka, 2014).

From these scenario ruptures, synthetic waveforms can be generated at the locations of operational seismic instrumentation, providing realistic data for testing operations. Using a deterministic approach (i.e., numerically solving the seismic wave equations in three dimensions) to generate synthetic waveforms that include both *P* and *S* waves allows consideration of complex path and site effects. Yet, the frequency content of generated waveforms is limited by our knowledge of earthquake source physics and fine-scale geologic structure, as well as by the high computing power required to perform such calculations (Rodgers *et al.*, 2018). Instead, broadband ground-motion simulations typically rely on a semistochastic approach in which low-frequency (<1 Hz) simulations are computed deterministically with either a 1D or 3D Earth structure and supplemented at high frequencies using a semistochastic approach (e.g., Pitarka *et al.*, 2000). In this method, the high-frequency content is obtained by building a prescribed source amplitude spectrum for each subfault based on known source theory, and convolving it with frequency-dependent site effects and path effects between the subfault and site. This total amplitude spectrum is then assigned a random phase to simulate the unknown complexities of the rupture and propagation. Originally developed for point-source applications (Boore, 1983), the semistochastic method has expanded to include finite-fault kinematics (e.g., Liu *et al.*, 2006; Graves and Pitarka, 2010; Mai *et al.*, 2010) and evaluated to compare subfault source time function parameterizations (e.g., Mena *et al.*, 2010; Melgar *et al.*, 2016).

Historically, high-frequency stochastic simulations designed for use in ground-motion models (e.g., Aagaard *et al.*, 2008, 2010) and structural response studies (e.g., Muto and Krishnan, 2011) have not included the contribution of the lower amplitude *P* wave, presumably due to its smaller effect on ground-motion parameters relevant to those applications. However, broadband *P* waves are a necessity for EEW system performance testing, since event detection and all of the first alerts in EEW systems (e.g., within ShakeAlert) are generated from algorithms that measure attributes of these initial *P* waves. Recently, the semistochastic method for synthetic seismograms has been adapted to include *P* waves (e.g., Ruhl *et al.*, 2017; Frankel *et al.*, 2018; Wirth *et al.*, 2018); however, we are not aware of any formal validation of synthetic *P* waves that confirms their utility for testing of EEW methods. To that end, we present an approach for the generation of synthetic seismic waveforms using a combination of deterministic and stochastic methods to create a broadband seismogram that includes physically realistic *P* waves. We validate these broadband waveforms in two ways: (1) we create rupture models based on the 2014 M_w 8.1 Iquique, Chile, earthquake and generate their associated synthetic seismograms. We compare these to strong-motion (accelerometer) observations in both the time and frequency domains and verify that the *P*-wave amplitude growth in the first 10 s mimics that of the observations; (2) we produce broadband synthetic waveforms for a suite of scenario rupture events for the CSZ ranging from magnitude 7 to 9. We compare to previous evaluations of *P*-wave amplitude growth patterns (Trugman *et al.*, 2019) and demonstrate with these validations that our broadband, semistochastic, synthetic seismograms are physically realistic and can therefore be integrated into testing for early warning ground-motion applications. The code used to generate these broadband waveforms is freely available (see Data and Resources).

CASE STUDY: 2014 M_w 8.1 IQUIQUE, CHILE, EARTHQUAKE

We describe our methodology using the 1 April 2014 M_w 8.1 Iquique, Chile, earthquake as an example. This earthquake occurred on the megathrust in which the Nazca plate subducts beneath the South American plate to its east. The event produced a 2 m tsunami and was observed in the nearfield by seismic stations operated by the Plate Boundary Observatory Network Northern Chile and the Red Sismológica Nacional. Shaking reached a peak ground acceleration (PGA) of ~60%*g*, or a modified Mercalli intensity of VIII, classified as severe shaking. Slip models generally show one main asperity with maximum slip between 4 and 8 m (Lay *et al.*, 2014; Schurr *et al.*, 2014; Gusman *et al.*, 2015).

Scenario ruptures

We begin with the U.S. Geological Survey (USGS) published slip model for the M_w 8.1 Iquique, Chile, earthquake (Hayes, 2017), and resample the coarse grid (12 km × 10 km subfaults) to smaller subfaults measuring 2 km × 2 km (Fig. 1a). We use

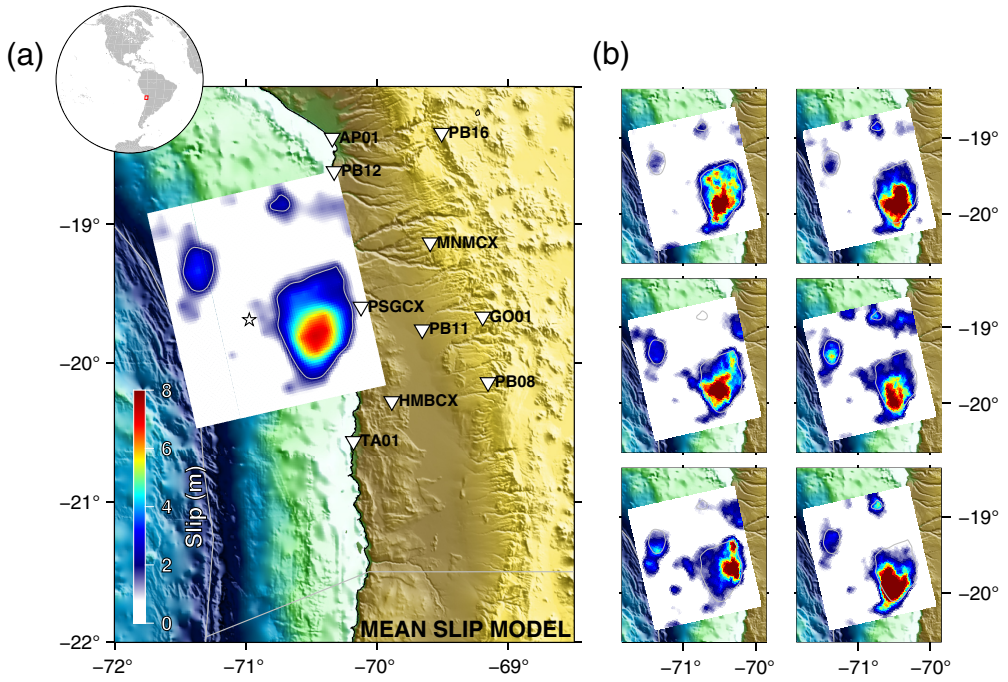

Figure 1. (a) Upsampled U.S. Geological Survey (USGS) slip model used as the mean model for the scenario rupture calculation. Major tectonic boundaries are given as gray lines, seismic stations included in our analysis are shown as white inverted triangles along with their four- or five-character station code. The event hypocenter is denoted by the white star. The 2 m slip contour is given by the gray lines. The inset globe at the top left shows the event location. (b) Six example stochastic slip distributions derived from mean model in panel (a). The 2 m contour from the mean slip model is superimposed over each of the stochastic slip distributions for spatial context. The remaining 34 stochastic slip distributions are available in Figure 2. The color version of this figure is available only in the electronic edition.

the upsampled slip distribution as a mean model from which to create 40 stochastic slip distributions using the K-L expansion method (LeVeque *et al.*, 2016; Melgar *et al.*, 2016). Mathematically, we assume that slip at each subfault is normally distributed with mean μ_k and standard deviation σ_k. The vector of total slip at each subfault, $\boldsymbol{s}$, is distributed as

$$\boldsymbol{s} \sim \mathcal{N}(\mu, \hat{\boldsymbol{C}}), \quad (1)$$

in which the mean vector μ is the resampled USGS slip model (Fig. 1a). Wavenumber domain methods generate many iterations of the stochastic slip distributions to find the random number seed that produces a visually comparable model to the reference slip inversion (e.g., Frankel, 2016). In contrast, by operating directly in the spatial domain, the K-L expansion approach produces stochastic models of which spatial features are mathematically linked to the base model, μ. The covariance matrix of the distribution, $\hat{\boldsymbol{C}}$, is a function of the standard deviation at each subfault and the correlation between each pair of subfaults. We use the von Karman correlation function, which has been demonstrated to best describe earthquake slip patterns (Mai and Beroza, 2002). The three parameters that define the von Karman correlation function are a slip roughness parameter (the Hurst exponent), and correlation lengths in the along-strike and down-dip direction, which control the size of slip asperities in each direction. We assign these parameters using empirical magnitude-dependent relations derived from earthquake catalogs of moderate-to-large magnitude events (Melgar and Hayes, 2019).

From the eigenvalues, λ_k, and eigenvectors, ν_k, of the covariance matrix, $\hat{\boldsymbol{C}}$, the K-L expansion states that the vector of slip at each subfault is

$$s = \mu + \sum_{k=1}^{N} z_k \sqrt{\lambda_k} \nu_k, \quad (2)$$

in which z_k are normally distributed random numbers used as weights to each eigenmode such that $z_k \sim \mathcal{N}(0, 1)$ (see Melgar *et al.*, 2016, for full details). We impose a maximum slip value of 15 m (roughly three times what is modeled in the USGS slip distribution) such that any resulting model with slip exceeding this value on a single subfault is discarded and recalculated. The result is, therefore, a series of slip distributions that generally share the qualities of the specified mean model, μ, the USGS slip inversion, plus some variation. We compute 40 such rupture scenarios (Figs. 1b and 2).

Synthetic waveforms

From the synthetic slip distributions (see the Scenario Ruptures section), we compute synthetic seismograms using a semistochastic approach, that is, a deterministic calculation at long periods and a reduced-physics random-phase approach at high frequencies. This is a well-known method (Graves and Pitarka, 2010, 2014), so we describe it here only generally, placing emphasis on which we deviate from what has been done before and the modifications we have added for *P*-wave synthesis.

Low-frequency simulation ($f < 1$ Hz). We first define the kinematic rupture parameters as in Graves and Pitarka (2010) with the modifications to subduction zones proposed by

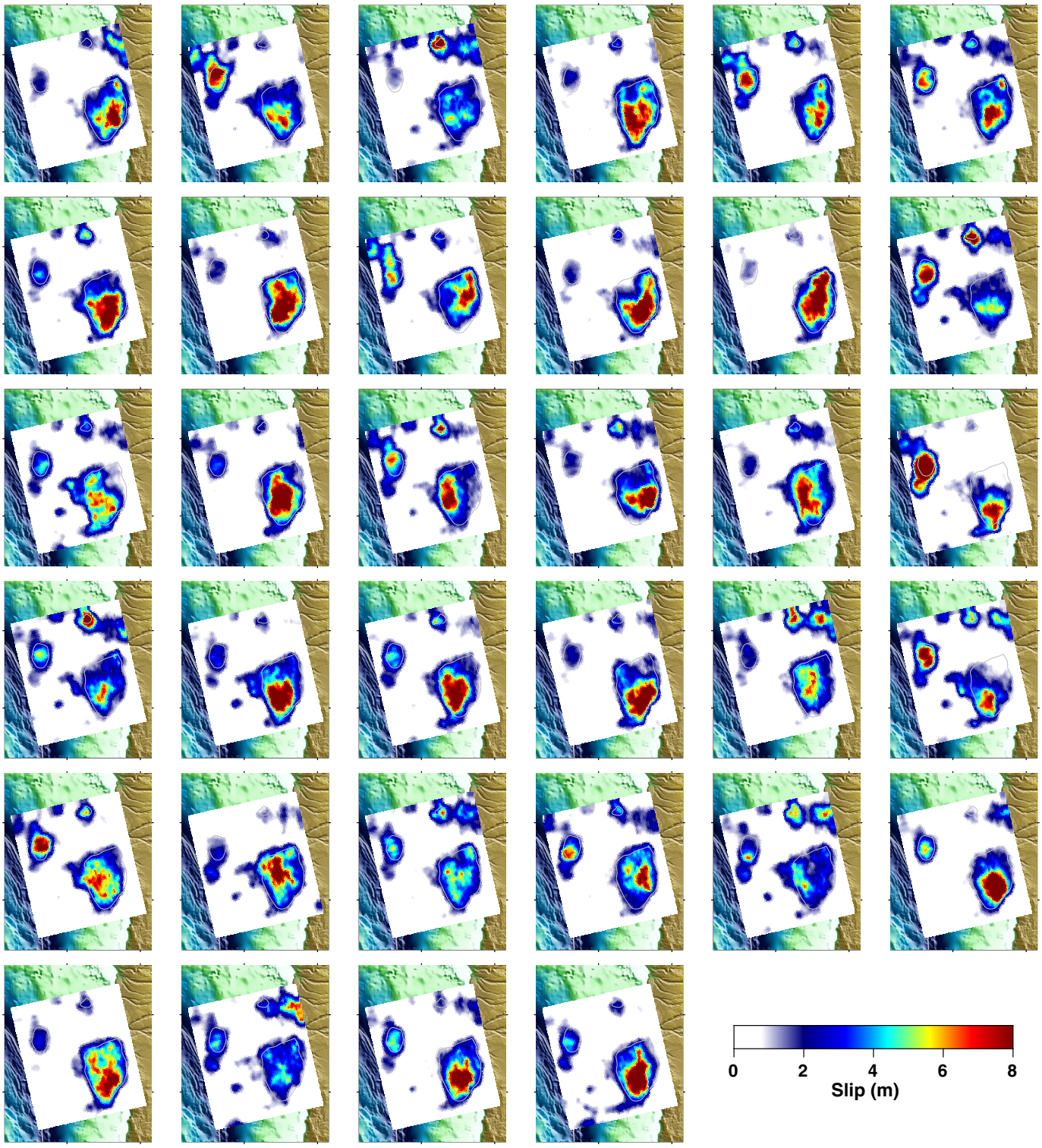

Figure 2. Remaining 34 of the total 40 stochastic slip distributions derived from the 2014 M_w 8.1 Iquique, Chile, mean model (Fig. 1). The 2 m contour from the mean slip model is superimposed over each of the stochastic slip distributions for spatial context. The color version of this figure is available only in the electronic edition.

Melgar *et al.* (2016). The background rupture speed, v_r, is defined as the piece-wise function:

$$v_r = \begin{cases} 0.49 \times v_s & d < 10 \text{ km} \\ 0.65 \times v_s & d > 15 \text{ km} \end{cases}, \quad (3)$$

in which v_s is the local shear-wave velocity, d is the depth of the subfault centroid, and a linear transition in rupture speed

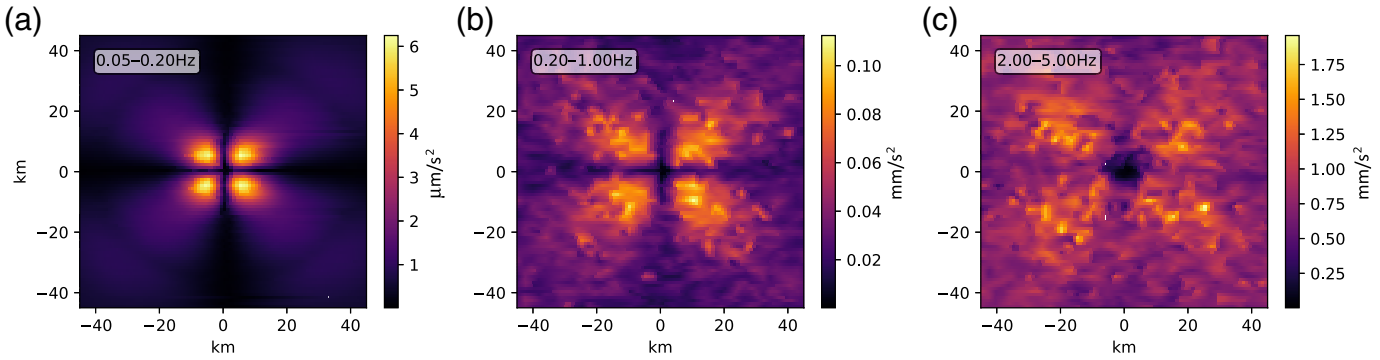

Figure 3. Peak amplitudes of the *P* wave for a vertical strike-slip point source at 10 km depth filtered at different narrow frequency bands. (a) 0.05–0.20 Hz, (b) 0.20–1.00 Hz, and (c) 2.00–5.00 Hz. The color version of this figure is available only in the electronic edition.

is applied between 10 and 15 km depth. We deviate slightly from the depths suggested by Graves and Pitarka (2010) for continental faults and apply the transitions at deeper depths for application to the subduction zone environment. These depths are roughly consistent with the transition from domain A to domain B observed worldwide (Ye *et al.*, 2016). From Melgar *et al.* (2016) and Graves and Pitarka (2010), the onset times at each subfault are perturbed from this background velocity to allow faster propagation in which slip is large and slower propagation in which slip is small, consistent with dynamic rupture models (e.g., Day, 1982). An additional perturbation is applied to this relationship to remove the perfect 1:1 ratio between slip amount and rupture speed. It is possible for this additional perturbation to assign rupture onset times prior to the passing *P*-wave front at those subfaults near the prescribed hypocenter. Thus, in our final step, we perform a check to identify whether these perturbations resulted in slip onset at any subfault prior to the passing *P*-wave front from the event origin, thus violating causality. If any subfaults are found to have been assigned an onset time that conflicts with this requirement, the random perturbation is applied repeatedly until it no longer violates that rule, up to 500 recalculations. If after 500 calculations no valid perturbed onset time is chosen, the subfault is assigned to its original, unperturbed onset time. This constraint also allows simple ray tracing of the *P*- and *S*-wave arrivals at any receiving station, since the first arrivals are known to come from the prescribed hypocenter subfault.

Following Graves and Pitarka (2010), the local duration of slip (rise time) at each subfault is scaled by the square root of slip, such that subfaults with more slip will rupture with longer rise times. Subfaults with centroid depths less than 10 km are assigned rise times twice the duration of a subfault with the same slip amount at >15 km depth, with a linear transition from 10 to 15 km depth. We parameterize slip by the Dreger slip-rate function (Dreger *et al.*, 2007; Mena *et al.*, 2010; Melgar *et al.*, 2016):

$$\dot{s} = t^{-\zeta} e^{-t/4\tau}, \tag{4}$$

in which $\zeta = 0.2$, and 4τ is the local rise time (Melgar *et al.*, 2016). The ζ parameter controls the sharpness of onset of the slip-rate function, and the coefficient applied to τ controls the steepness of its decline.

The deterministic approach used to compute the long-period portion of our synthetic waveforms includes both *P* and *S* waves. We build a Green's function matrix using a 1D velocity model (Laske *et al.*, 2013) and a frequency–wavenumber (*f*-*k*) integration algorithm (Zhu and Rivera, 2002) to compute impulse responses for every receiver station to subfault pair in three components of motion: east, north, and up. This impulse response is then convolved with a subfault-specific slip-rate function calculated from equation (4), in which the rise time, 4τ, is proportional to the square root of slip. Once fully assembled for each subfault-to-station pair, the Green's function matrix is multiplied by the slip vector, $\boldsymbol{s}$, to calculate the low-frequency three-component waveforms. We note that the *f*-*k* integration algorithm introduces small-amplitude computational noise in the resulting Green's functions as a result of the inverse Fourier transform (Zhu and Rivera, 2002), including prior to the modeled seismic-wave arrival. For large events with many subfaults, the cumulative effect of the pre-event noise from many subfaults causes improper measurement of the *P* wave. To avoid complication in accurately measuring the *P* wave, we zero out the Green's function waveforms in the pre-event time window (TW).

High-frequency simulation ($f > 1$ Hz). The high-frequency component of the synthetic waveforms is calculated with a semistochastic method following Graves and Pitarka (2010) in which each subfault contributes an *S*-wave acceleration spectrum, $A_i^S(f)$, expressed by

$$A_i^S(f) = \sum_{j=1,M} C_{ij}^S S_i(f) G_{ij}(f) P(f), \tag{5}$$

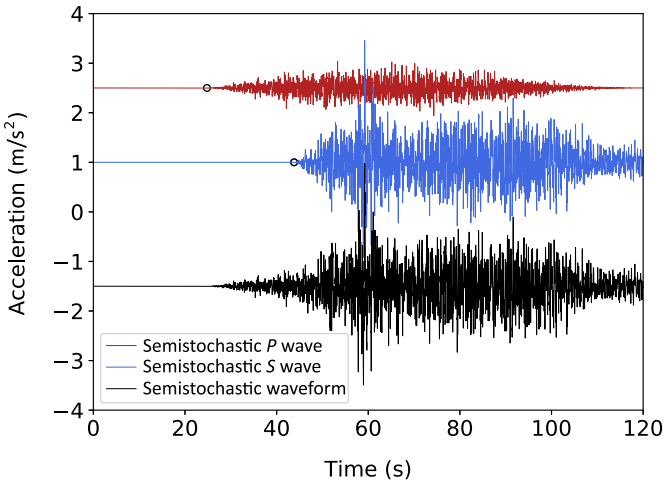

Figure 4. Example output of high-frequency ($f > 1$ Hz) semistochastic simulation including *P*-wave packet (red), *S*-wave packet (blue), and their sum (black). Black circles on the *P*- and *S*-wave packets represent the theoretical *P*- and *S*-wave arrival times, respectively, from ray tracing through the 1D velocity model. Waveforms are vertically offset for visual clarity. The color version of this figure is available only in the electronic edition.

in which S_i is the source-radiation spectrum, G_{ij} is the path term, P is the high-frequency spectral decay, and C_{ij}^S is the *S*-wave radiation scale factor given by

$$C_{ij}^S = \frac{F_s R_{Pij}^S}{4\pi\rho_i\beta_i^3}. \quad (6)$$

$F_s = 2$ accounts for free surface amplification, R_{Pij}^S is a conically averaged *S*-wave radiation pattern term, ρ_i is the density at the centroid of the subfault, and β_i is the shear-wave velocity at the centroid of the subfault. We extend this logic to include a *P*-wave packet by calculating the acceleration spectrum, $A_i^P(f)$, in which the radiation scale factor is calculated instead for the *P* wave, C_{ij}^P, given by

$$C_{ij}^P = \frac{F_s R_{Pij}^P}{4\pi\rho_i\alpha_i^3}, \quad (7)$$

in which R_{Pij}^P is a conically averaged *P*-wave radiation pattern term, and α_i is the compressional-wave velocity at the centroid of the subfault. Similarly, we use the *P*-wave quality factor in the path calculation. The source-radiation spectrum, S_i, does not refer to an *S*-wave-specific term, despite the nomenclature. We have adopted the same nomenclature as Graves and Pitarka (2010) and refer the reader to that work for additional information. We follow the same approach that Graves and Pitarka (2010) employed for defining the *S*-wave radiation pattern and extend it to the *P*-wave radiation pattern. The approach produces a gradual transformation of the radiation pattern from anisotropic to isotropic above a threshold of about 1 Hz. This relaxation of radiation pattern effects is supported by observations (e.g., Takemura *et al.*, 2009). Figure 3 shows the effects of this for the *P*-wave component for ground motion using the peak amplitudes of the *P* wave for a vertical strike-slip point source at 10 km depth filtered at different narrow frequency bands. At long periods, the theoretically expected four-lobed pattern is clearly visible. As the frequencies approach 1 Hz, the pattern begins to break down. At frequencies higher than 1 Hz, it is almost indiscernible.

We take the inverse Fourier transform of $A_i^S(f)$ and $A_i^P(f)$ to create the *S*- and *P*-wave packets and sum them in the time domain to obtain the full high-frequency (100 Hz) portion of the waveform (Fig. 4). We note that we have used site amplification factors consistent with the quarter-wavelength approximation (Boore and Joyner, 1997), which were designed for *S* waves, for calculation of G_{ij} in both A_i^S and A_i^P. We discuss this choice in the Discussion section.

Broadband simulation. Finally, we combine the low-frequency and high-frequency simulations by calculating the sum of the two after a matched filtering process. First, we take the second derivative of the long-period waveforms to convert from displacement to acceleration and apply a fourth-order, causal, low-pass filter with a corner frequency of 1 Hz. Next, we apply a fourth-order, causal, high-pass filter with a corner frequency of 1 Hz to the high-frequency acceleration waveforms (Kamae *et al.*, 1998). The waveform resulting from the sum of these two quantities (e.g., Fig. 5), therefore, has the characteristics of the low-frequency simulation (see the Low-Frequency Simulation ($f < 1$ Hz) section) at frequencies below 1 Hz, and those of the high-frequency simulation (see the High-Frequency Simulation ($f > 1$ Hz) section) at frequencies above 1 Hz.

Validation

Although it is not the objective of the study to validate the strong motions generated by our code, prior to showing the *P*-wave results, we will briefly show that the method produces reasonable ground-motion simulations. We compare the performance of our synthetic waveforms to the observed accelerometer waveforms in the frequency domain (e.g., Fig. 6a) to establish agreement in the spectral accelerations across frequencies of interest, from 0.1 Hz to the Nyquist frequency, 50 Hz, and for PGA. We calculate the residual at each frequency of interest, defined as the natural logarithm of the ratio between observed and predicted spectral accelerations (Fig. 6b). Ideally, we aim for synthetics with a similar mean to the observations, but with a greater spread, to allow for variation between the mean model (the true Iquique earthquake slip distribution) and our varying synthetic rupture scenarios. Generally, our agreement is good, especially at frequencies above 1 Hz, demonstrating the robustness of our semistochastic waveform generation. The deterministic portion of the waveform generation controls the fits at lower frequencies (<1 Hz).

To obtain agreement at the lower frequencies ($f < 1$ Hz), we used a mean rise time of 3.92 s, which is 45% of the mean

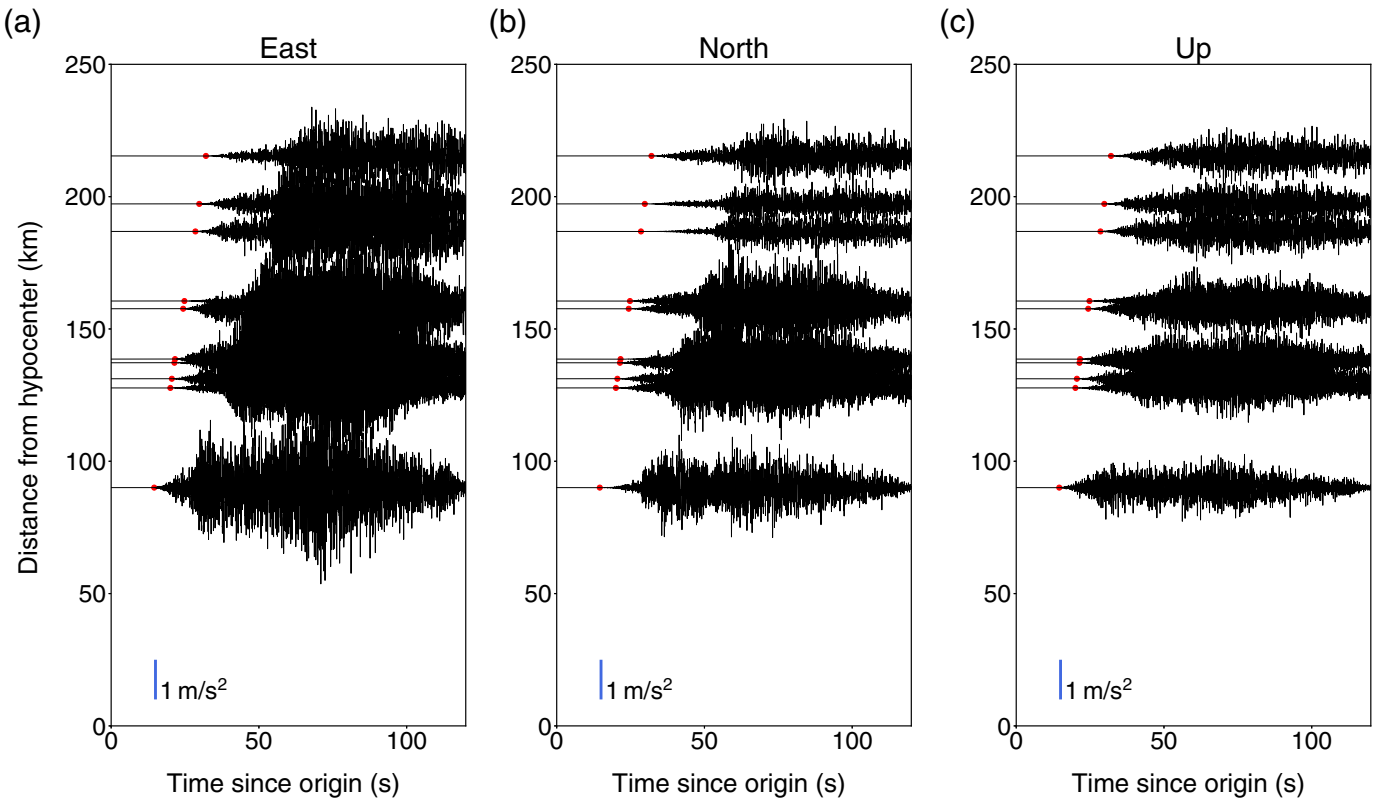

Figure 5. Example broadband (up to 100 Hz) synthetic waveforms in three components (a: east, b: north, and c: up) at 10 receiver stations between 90 and 220 km hypocentral distance for a single-scenario rupture model. The waveforms include both an *S*-wave and *P*-wave packet. Red dots denote the independently calculated *P*-wave arrival time from ray tracing through the prescribed 1D velocity model (Laske *et al.*, 2013). The color version of this figure is available only in the electronic edition.

value predicted by Melgar and Hayes (2017). The positive bias at low frequencies suggests that the values predicted by our deterministic approach are low compared to the observations. The mean residual is slightly larger than 0.5 ln units between 0.2 and 0.5 Hz, indicating that additional tuning of the parameters relevant to the deterministic waveform generation could be considered, if the user's scientific goals require it. This bias could be due to a number of model parameters, including the velocity structure and the choice of source time function parameterization (equation 4). We are primarily concerned with the added feature of the high-frequency *P*-wave portion of the synthetic waveforms, for which the spectral accelerations of the modeled waveforms agree well.

We further evaluate the synthetic *P* waves in the time domain by comparing *P*-wave amplitude growth as a function of time to the observed data. We follow the waveform-processing method described in Trugman *et al.* (2019), which demonstrated that there is a predictable evolution of *P*-wave displacement in the first tens of seconds of rupture. In that study, the observed acceleration waveforms were processed as follows:

1. De-mean accelerations,
2. High-pass filter accelerations to 0.075 Hz,
3. Double integrate accelerations to displacement,
4. Band-pass filter resulting displacements between 0.075 and 3.0 Hz,
5. Truncate waveforms at 95% of the inferred *S*-wave arrival time to avoid measuring the *S* wave,
6. Measure peak displacement amplitude, P_d, in various TWs following the *P*-wave arrival,
7. Correct P_d to a reference distance of 10 km.

Following these steps, we find agreement between our synthetic results and observed data. That is, over the first 10 s of observation, our simulated *P* waves for the Iquique earthquake grow in amplitude at a rate consistent with observations (Fig. 7). We employ a Welch's *t*-test to validate the synthetic *P*-wave amplitudes against the observed dataset. A Welch's *t*-test is designed to test the hypothesis that two populations have equal means and is appropriate for comparison when the two datasets have unequal sample sizes and variances. As before, we aim for our synthetic dataset (400 samples) to have a similar mean but larger variance than our observed dataset (10 samples), making the Welch's *t*-test the appropriate validation metric. The Welch's *t*-test confirms consistency between the two distributions ($p > 0.05$ at all time steps). In fact, in the observation window most often used for *P*-wave amplitude scaling in EEW (3–5 s), $p > 0.45$ indicating good agreement of our synthetic *P* waves to

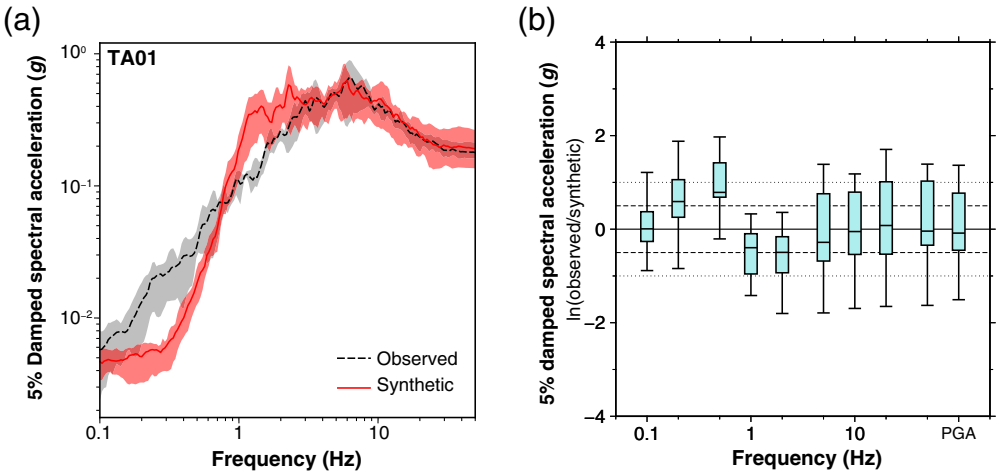

Figure 6. (a) Example 5% damped spectral acceleration for observed acceleration waveform (dashed black) at station TA01 and synthetic waveform (solid red) from one of the scenario events (Fig. 1b). The solid lines denote the 50th percentile, with shaded regions denoting the range from 0th to 100th percentile. (b) 5% damped spectral acceleration (50th percentile) residual (natural logarithm of the ratio of observed to synthetic spectral acceleration) at various frequencies and peak ground acceleration (PGA) for each of the 10 stations and 40 scenario ruptures. Dashed lines are shown at residuals of ±0.5 ln units and dotted lines at residuals of ±1.0 ln units. The color version of this figure is available only in the electronic edition.

the observed waveforms. We note that because we have not included site effects in our analysis, these results represent an oversimplification of real observations.

P-WAVE AMPLITUDE CHARACTERISTICS: CASCADIA EXAMPLE

Upon confirmation of agreement in both the time and frequency domains, we transition now to evaluate the *P*-wave

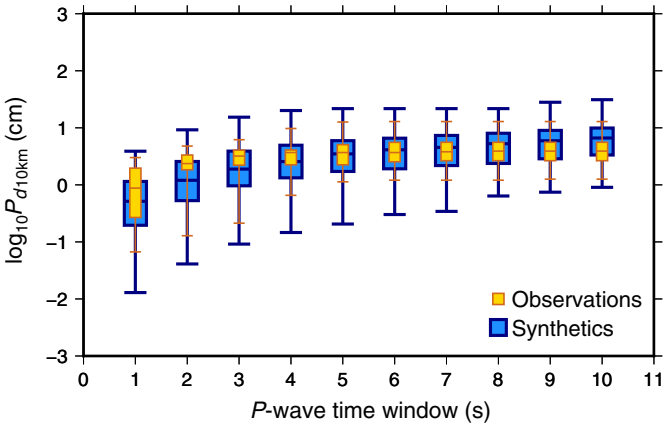

Figure 7. Comparison of synthetic *P*-wave amplitudes (wide blue box and whiskers) behind observed amplitudes (thin yellow box and whiskers) from the 2014 M_w 8.1 Iquique earthquake in the first 10 s of observation. Waveform amplitudes have been corrected to a reference distance of 10 km. Synthetic data include 400 observations in each box and whisker (40 scenario events and 10 stations each), whereas observed data include 10 data points (one per station) in each box and whisker. The color version of this figure is available only in the electronic edition.

packet more fully, including across a range of magnitudes, $7.0 \le M_w \le 9.0$. We follow Melgar *et al.* (2016) to create synthetic rupture scenarios for the CSZ using the Slab2 geometry (Hayes *et al.*, 2018) with a down-dip limit of slip of 25 km (Fig. 8). We consider only the portion of the slab south of British Columbia, Canada, simply to reduce the computational load, and because there are currently more sites in Oregon and Washington than on Vancouver Island. We discretize this slab geometry into 6643 triangular subfaults using a finite-element mesher (Geuzaine and Remacle, 2009). Unlike in the Iquique case (see the Scenario Ruptures section), because details of the future rupture are unknown, we begin with a mean slip model consisting of homogeneous slip across the slab, scaled to produce an earthquake of the magnitude of interest. We do not fix the hypocenter, rather the hypocenter is selected at random from within the fault-rupture area. The rupture dimensions for a given magnitude event are selected at random using the mean and standard deviation from published magnitude to rupture-size scaling laws (Blaser *et al.*, 2010). We compute 10 ruptures for each magnitude from 7.0 to 9.0 at intervals of 0.1 magnitude units. For testing the EEW capabilities of a system that needs to perform in a region for which limited present-day seismicity and historical data exist, this approach is appealing. Little is known about the next CSZ event, so we make as few assumptions as possible. Indeed, our only assumptions are (1) that the next CSZ earthquake will have slip that follows the same von Karman correlation magnitude-dependent statistics as other worldwide great subduction zone events (Melgar and Hayes, 2019), and (2) that there is a 25 km depth down-dip limit for slip. We emphasize how little is known about the next CSZ event; therefore, our goal is not to forecast what are the likely features of the next CSZ event but rather to generate events with a large breadth of variability that can expose where a system is performing well and where it is challenged. The statistics describing the features of our resulting scenario ruptures are available in Figure 9. Following generation of the ruptures, we compute synthetic waveforms at the locations of 30 currently operational strong-motion seismic stations (Fig. 8) selected simply to sample a range of distances and azimuths. We use a 1D velocity model (Gregor *et al.*, 2002) for the long-period portion of the waveforms and complete our waveform

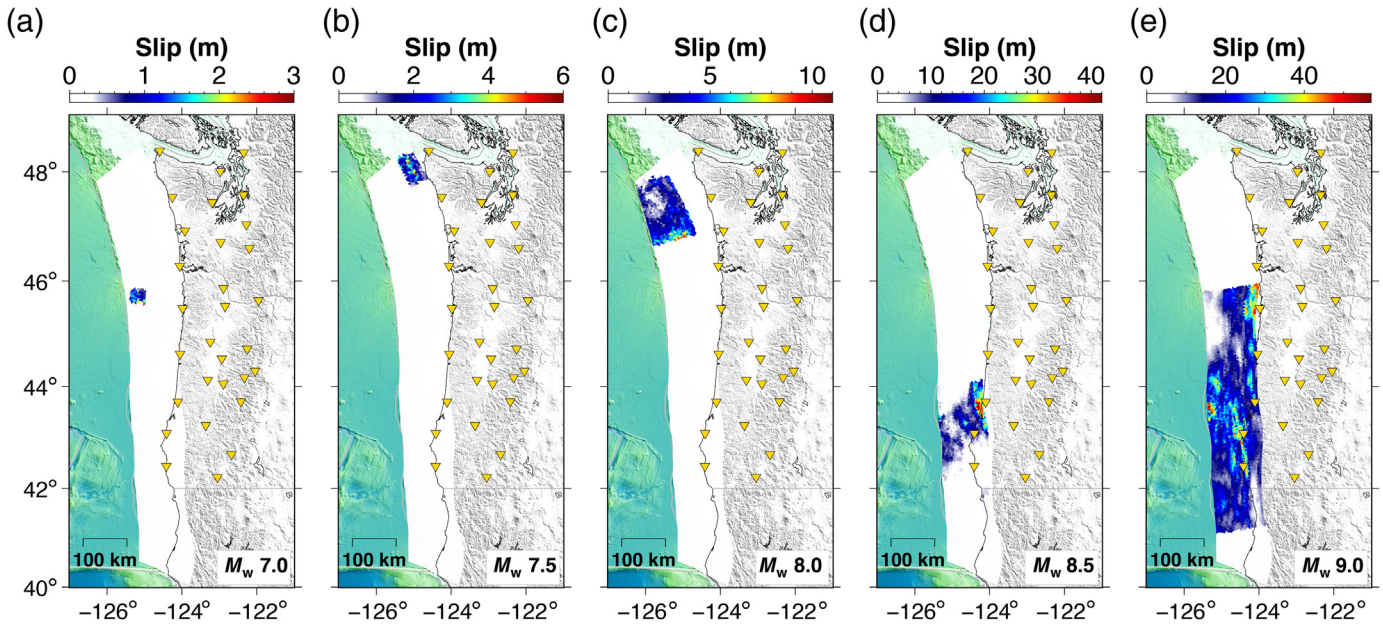

computation following the procedure described in the Synthetic Waveforms section.

Once again, we process the synthetic waveforms in the manner described in the earlier Validation section and compare the time-dependent growth of *P*-wave amplitudes in our synthetic waveforms to observed data, this time using the Japan-area dataset analyzed by Trugman *et al.* (2019). We use a Markov chain Monte Carlo (MCMC) approach to solve for the slopes, *y* intercepts, and intersection point of two straight lines to describe the complete dataset composed of the observations analyzed by Trugman *et al.* (2019) and the synthetic waveforms generated in this study. The intersection point of these two lines represents the saturation magnitude (see Fig. 10). The prior distributions of the two slopes and one *y* intercept are given as normal probability distributions, with a sampling space between 0 and 2 for low-magnitude slope, 0 and 1 for the high-magnitude slope, and −20 to 0 for the low-magnitude *y* intercept. We use a uniform distribution as the prior for the intersection magnitude, with a sampling space between M_w 5 and M_w 8. The *y* intercept of the high-magnitude regression is dependent on the other four parameters to have the two lines intersect and is therefore computed afterward. We estimate the posterior distribution using four Markov chains with a Metropolis–Hastings criterion. We use a total of 3500 samples for each Markov chain, in which the first 500 are burn-in samples that are not used for posterior estimation, resulting in 3000 useful samples per Markov chain, and, therefore, 12,000 samples of the posterior distribution. To apply equal weight to each sampled magnitude, we consider the average *P*-wave amplitude at every 0.1 magnitude unit in our analysis. Figure 10 shows the results of the MCMC approach, with the two linear regressions in gold, the intersection point and 1σ uncertainty shown as a solid vertical line and gray shaded region.

Figure 8. Example Cascadia subduction zone scenario ruptures for (a) M_w 7.0, (b) M_w 7.5, (c) M_w 8.0, (d) M_w 8.5, and (e) M_w 9.0. Note the different color scale above each subplot. Station locations used for analysis are shown as gold inverted triangles. The white region at the coastline overlain by the example slip distributions shows the slab geometry on which we calculated the scenario ruptures. The slab geometry comes from Slab2 (Hayes *et al.*, 2018), with a down-dip extent of 25 km and a northward extent limited at the southern edge of British Columbia to reduce the computational load. Note that these scenario ruptures are a single example from the random distribution of rupture dimensions at the target magnitude and are not to be considered representative of all scenarios at that magnitude. For a full view of the rupture statistics, see Figure 9. The color version of this figure is available only in the electronic edition.

From the previous analysis, we find that our synthetic seismograms follow the same saturation behavior predicted by Trugman *et al.* (2019) (dashed vertical line in Fig. 10). Peak *P*-wave displacement amplitudes for the magnitudes considered ($7.0 \le M_w \le 9.0$) are above the saturation magnitude until a TW > 6.0 s. By TW = 12.0 s, *P*-wave amplitude exhibits magnitude-dependent scaling up to ~M_w 7.4. By 20 s, *P*-wave amplitude is consistent with overall magnitude saturation, in which events larger than about M_w 7.5 remain impossible to differentiate. Although there is a slight positive slope above the magnitude saturation point, it is markedly shallower than the *P*-wave scaling laws anticipate. In an EEW setting, the *P*-wave amplitudes of an M_w 7.5 and M_w 9.0 event would be virtually indistinguishable. Trugman *et al.* (2019) noted that the M_w 9.0 Tohoku-Oki event is an outlier to their predicted *P*-wave amplitude growth. Our synthetic events confirm this point; although the average amplitude of the Tohoku event is only 1.2 standard deviations below the average synthetic M_w 9.0 event at TW = 1 s, this difference grows to 2.9 standard

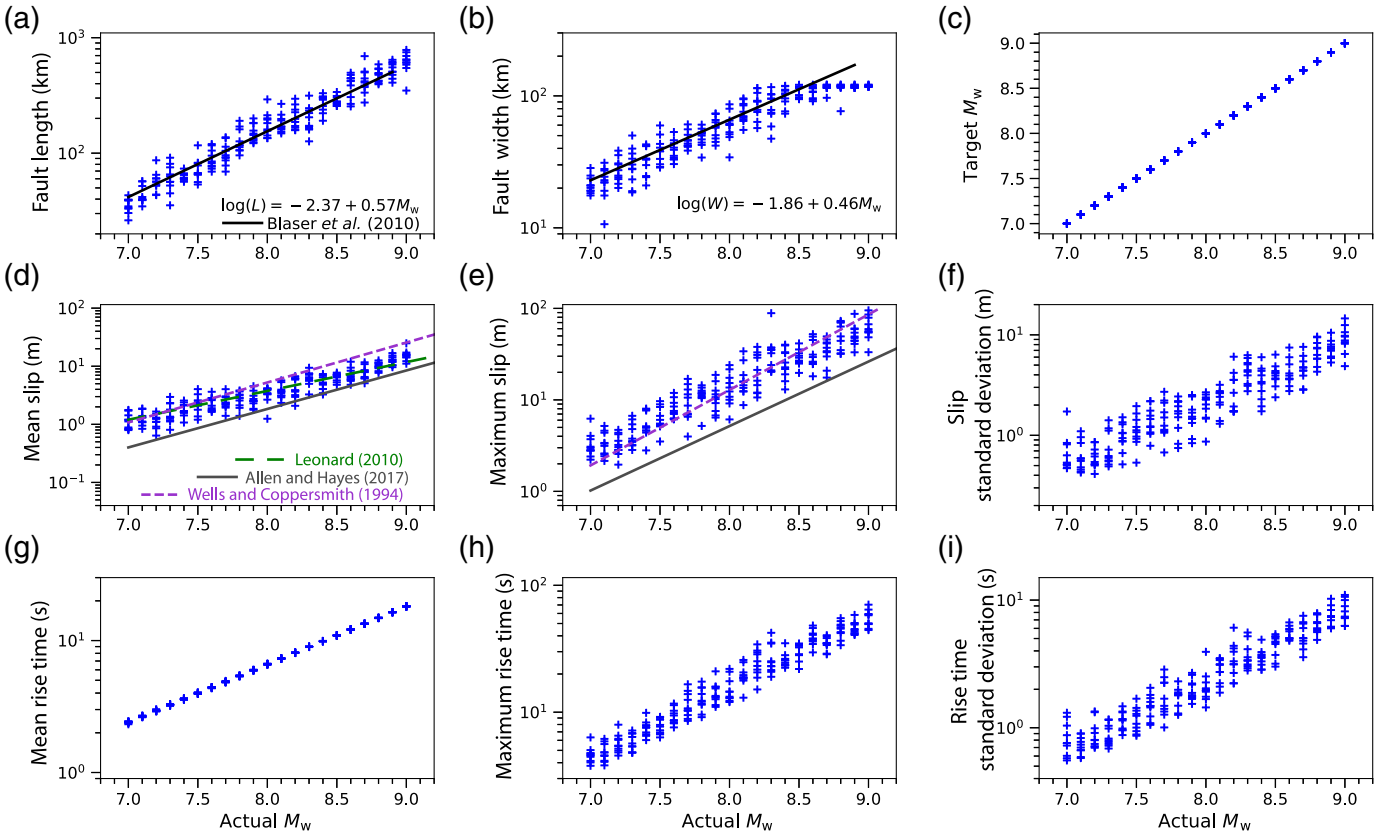

Figure 9. Statistics of scenario ruptures: (a) fault length, (b) fault width, (c) target magnitude, (d) mean slip, (e) maximum slip, (f) standard deviation of slip, (g) mean rise time, (h) maximum rise time, and (i) standard deviation of rise time versus event magnitude. Panels (a) and (b) show scaling laws from Blaser *et al.* (2010) (black lines). Panels (d) and (e) show scaling laws from Leonard (2010) (long green dashes), Allen and Hayes (2017) (solid gray line), and Wells and Coppersmith (1994) (short purple dashes). The color version of this figure is available only in the electronic edition.

deviations at TW = 4 s. By TW = 20 s, the Tohoku event exhibits amplitudes more consistent with our synthetic waveforms and the pattern predicted by Trugman *et al.* (2019), returning to within one standard deviation of the mean synthetic event.

DISCUSSION

The broadband seismograms constructed with the semistochastic methodology, and including *P* waves, are physically realistic; they are in agreement with *P*-wave observations, in particular, *P*-wave amplitude growth in the time domain. With the K-L expansion method, and using the 2014 M_w 8.1 Iquique, Chile, slip model as our mean model, we constructed a suite of scenario ruptures that share similar spatial features to the true event, allowing a fair comparison between the observed seismic waveforms and those calculated semistochastically from our scenario ruptures. Assigning a mean rise time of 3.92 s, we achieved satisfactory agreement across frequencies of interest. In the time domain, we demonstrated that the evolution of the modeled *P*-wave amplitudes mimics that of the observations.

We also find that this approach produces *P* waves that are consistent with previously identified patterns of *P*-wave amplitude growth across moderate-to-large magnitudes, using rupture scenarios for the CSZ to compare to *P*-wave growth patterns observed by Trugman *et al.* (2019). Our results demonstrate that this tool successfully generates physically realistic, broadband seismograms with *P* waves typical of real earthquakes. This work is the first formal validation of semistochastic *P* waves and confirms the appropriateness of our synthetic waveform generation tool for EEW testing. We suggest that similar tools used to generate *P*-wave arrivals (see Introduction) can be validated using the same procedures applied here and included in EEW testing thereafter.

P-wave characteristics in both the time and frequency domains are critical for EEW applications. Not only are *P*-wave arrivals used to initiate EEW procedures, the qualities of the early seconds of *P* waves (e.g., dominant period and amplitude) are used to estimate earthquake source parameters that inform early warning and rapid response products. The algorithms implemented in EEW systems such as ShakeAlert in the United States always rely first on estimates of earthquake magnitude from a simple point-source scaling relation between hypocentral distance and *P*-wave displacement amplitude

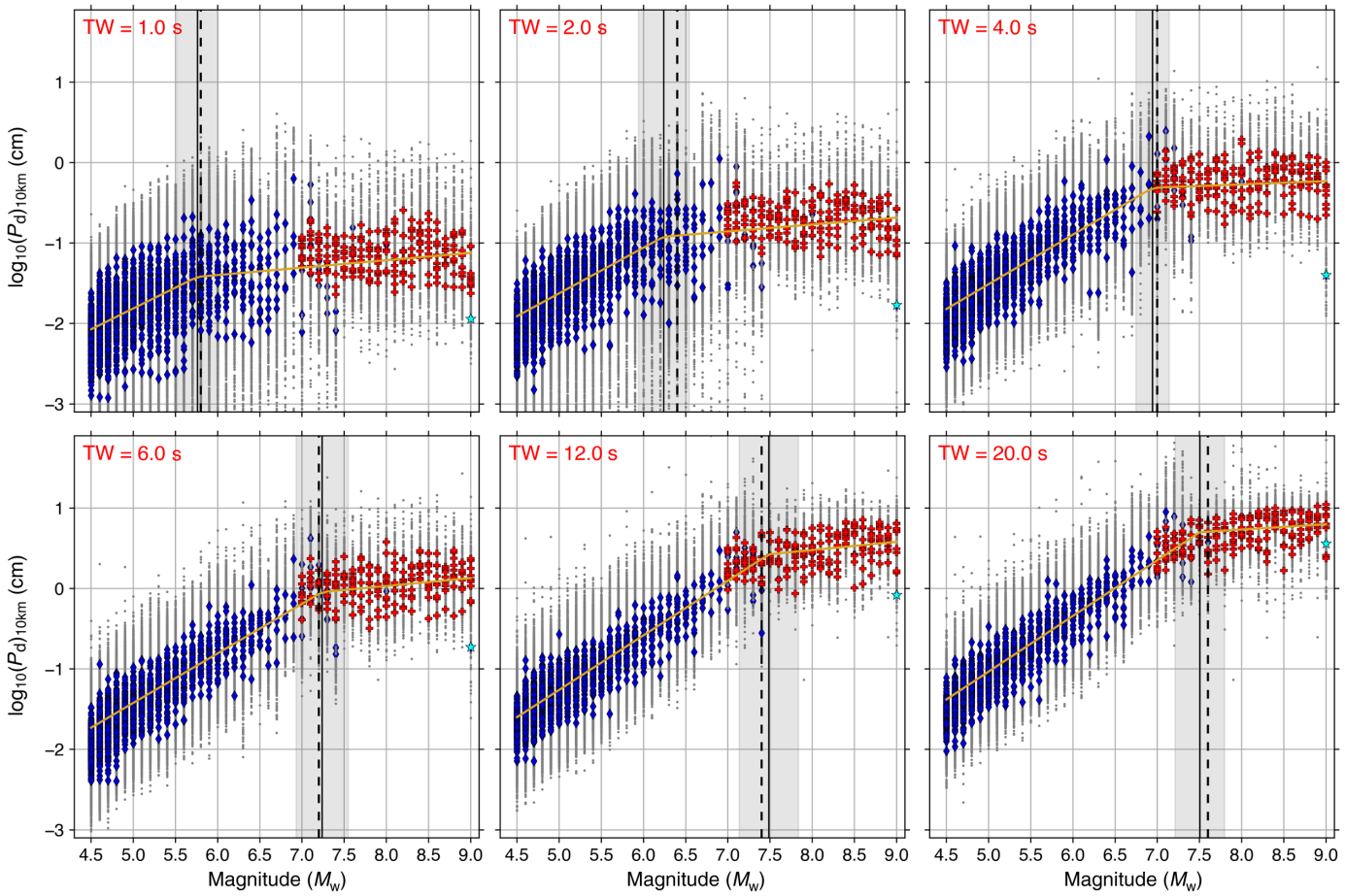

Figure 10. *P*-wave displacement amplitude corrected to a hypocentral distance of 10 km for TWs of 1, 2, 4, 6, 12, and 20 s after *P*-wave arrival. Data from Trugman *et al.* (2019) are shown as blue diamonds, and data from this study are shown as red pluses. The M_w 9.0 Tohoku-Oki event from Trugman *et al.* (2019) is shown as a cyan star. The diamonds, pluses, and star denote the mean value for a single earthquake (mean of all observing stations), whereas each gray dot represents a single station observation. The solid gold line shows the best-fitting set of two straight lines from the Markov chain Monte Carlo approach discussed in the *P*-wave Amplitude Characteristics: Cascadia Example section. The solid, black, vertical line, and the gray shaded region denotes the slope transition point (i.e., the upper limit of reliable magnitude scaling) and 1σ uncertainty. The dashed vertical line denotes the magnitude at which Trugman *et al.* (2019) identified saturation. The color version of this figure is available only in the electronic edition.

(Chung *et al.*, 2019). This method is reliable at magnitudes below about M_w 7.5 and is subject to magnitude saturation above this size (Fig. 10, Hoshiba *et al.*, 2011; Trugman *et al.*, 2019). The Japan Meteorological Agency issued an early warning for the 2011 M_w 9.0 Tohoku-Oki earthquake using a similar method, resulting in a magnitude estimate that saturated at M_w 8.1. Using one of the M_w 9.0 scenario ruptures from the CSZ (Fig. 11a,b), we demonstrate a similar result that considers the simulated real-time magnitude estimate using the magnitude scaling relation of Kuyuk and Allen (2013). Using only the first 4 s of observation after the *P* wave (pink line in Fig. 11c), the magnitude estimate stops growing at $\sim M_w$ 6.5. Using all available *P*-wave data (purple line in Fig. 11c), the *P* waves calculated from our scenario rupture result in a similar temporal evolution of the magnitude estimate that was exhibited in real time during the Tohoku-Oki event (blue line in Fig. 11c) (Minson *et al.*, 2018).

Following the Tohoku-Oki event, the EEW community has recognized the value of geodetic observations to avoid magnitude saturation and provide reliable estimates of the earthquake source size in the first minutes after event origin (e.g., Melgar *et al.*, 2015; Ruhl *et al.*, 2017; Murray *et al.*, 2018). Synthetic displacements generated with the deterministic method applied here were previously validated against high-rate Global Navigation Satellite Systems (HR-GNSS) observations (Melgar *et al.*, 2016), demonstrating that geodetic early warning algorithms (e.g., peak ground displacement magnitude estimation) can be reliably tested with these methods as well. With the current study, we can now test a fully hybrid system, including both synthetic HR-GNSS and strong-motion seismic datasets. Furthermore, performance analysis of these different approaches, specifically their ability to provide timely forecasts of strong shaking before it occurs, is becoming commonplace and is driving vigorous debate on how EEW systems should operate in the future (Ruhl *et al.*, 2019; Meier *et al.*, 2020; Wald, 2020). Data for large earthquakes are scant and so

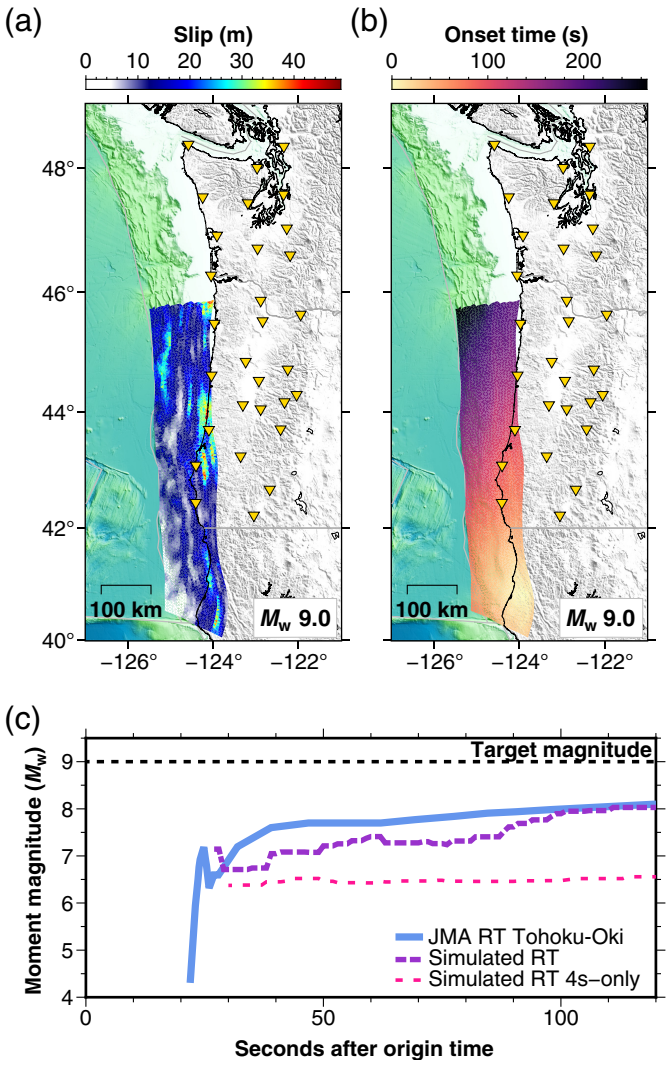

Figure 11. Earthquake early warning example for an M_w 9.0 scenario event. (a) Slip model, (b) rupture onset times along fault, and (c) simulated real-time (RT) *P*-wave amplitude magnitude estimate using only the first 4 s after *P*-wave arrival (pink, dotted line) and using all available data prior to the *S*-wave arrival (purple, dashed line), with the real-time Japan Meteorological Agency (JMA) magnitude estimate for the 2011 M_w 9.0 Tohouku-Oki earthquake (blue, solid line) as a reference. The target magnitude, M_w 9.0, is given as a black dashed line. The color version of this figure is available only in the electronic edition.

simulation approaches that can accurately replicate operationally important aspects of a seismogram are particularly valuable.

The code developed to generate the synthetic waveforms presented here is freely available (see Data and Resources) and includes options for varying parameters to simulate specific rupture qualities (e.g., hypocentral location, asperity size, and local rupture duration) as well as parameters that affect the resulting synthetic waveforms (e.g., attenuation parameters, source time function parameterization, and rupture velocity). Adjustment to these parameters will allow continuous improvement to these models of high-frequency seismograms based on new analyses or newly available observations of large events. For example, we noted in the High-Frequency Simulation ($f > 1$ Hz) section that we have used site amplification factors designed for *S* waves (Boore and Joyner, 1997), throughout our high-frequency simulations. Our *P*-wave amplitudes behave as expected using this assumption, and thus we find this approximation useful for our purposes. However, we consider the integration of site amplification analyses specific to *P* waves to be an important area for future improvement. We also note that the focus of this work is *P*-wave amplitude validation. We have performed only a limited validation for the strong shaking portions of the resulting synthetic seismograms by comparison against the M_w 8.1 Iquique earthquake recorded waveforms. Although those results are encouraging, more validation of this tool against ground-motion models and observations from other events is still required and is part of our ongoing work.

CONCLUSIONS

We present an approach for generating stochastic scenario rupture models and associated high-rate seismic waveforms for the application of early warning systems testing and refinement. We have demonstrated the benefits of the K-L expansion approach for generating scenario ruptures directly in the spatial domain, as it allows input of a base model that serves as the mean slip distribution for scenario events. Using this approach, it becomes straightforward to create many synthetic slip distributions that share some desired spatial qualities, simplifying comparisons between real and synthetic earthquake slip distributions.

We also present validation of synthetic high-rate seismic waveforms, and particularly P-waves, using a semistochastic approach. We demonstrate agreement in the frequency domain, up to the Nyquist frequency of 50 Hz and in the time domain, showing that the synthetic *P*-wave amplitude growth follows observed behavior across magnitudes. Our validation suggests that the broadband synthetic seismograms we have calculated include physically realistic *P* waves and are useful for testing EEW procedures for large magnitude events, in which synthetic data are particularly valuable as a supplement to the small observational dataset.

DATA AND RESOURCES

The strong-motion accelerometer waveforms used in this study are from stations operated by the Plate Boundary Observatory Network Northern Chile and the Red Sismológica Nacional. Data can be obtained from the Incorporated Research Institutions for Seismology (IRIS) Data Management Center at www.iris.edu (last accessed January 2020). The scenario slip distributions and synthetic waveforms were created using the FakeQuakes module of the MudPy suite of source modeling and inversion codes. These codes can be obtained at http://www.github.com/dmelgarm/MudPy (last accessed May 2020).

ACKNOWLEDGMENTS

The authors would like to thank Daniel Trugman for his assistance with the dataset from Trugman *et al.* (2019). The authors would also like to thank Associate Editor Arben Pitarka and two anonymous reviewers for their thoughtful comments and suggestions. This work was funded by U.S. Geological Survey (USGS) Earthquake Hazards Program (EHP) Grant Number G19AP00010 and National Science Foundation (NSF) Grant Number OAC-1835661.

REFERENCES

Aagaard, B. T., T. M. Brocher, D. Dolenc, D. Dreger, R. W. Graves, S. Harmsen, S. Hartzell, S. Larsen, K. McCandless, S. Nilsson, *et al.* (2008). Ground-motion modeling of the 1906 San Francisco earthquake, part II: Ground-motion estimates for the 1906 earthquake and scenario events, *Bull. Seismol. Soc. Am.* **98,** no. 2, 1012–1046.

Aagaard, B. T., R. W. Graves, A. Rodgers, T. M. Brocher, R. W. Simpson, D. Dreger, N. A. Petersson, S. C. Larsen, S. Ma, and R. C. Jachens (2010). Ground-motion modeling of Hayward fault scenario earthquakes, part II: Simulation of long-period and broadband ground motions, *Bull. Seismol. Soc. Am.* **100,** no. 6, 2945–2977.

Allen, R. M., and D. Melgar (2019). Earthquake early warning: Advances, scientific challenges, and societal needs, *Annu. Rev. Earth Planet. Sci.* **47,** 361–388.

Allen, T. I., and G. P. Hayes (2017). Alternative rupture-scaling relationships for subduction interface and other offshore environments, *Bull. Seismol. Soc. Am.* **107,** no. 3, 1240–1253.

Blaser, L., F. Krüger, M. Ohrnberger, and F. Scherbaum (2010). Scaling relations of earthquake source parameter estimates with special focus on subduction environment, *Bull. Seismol. Soc. Am.* **100,** no. 6, 2914–2926.

Boore, D. M. (1983). Stochastic simulation of high-frequency ground motions based on seismological models of the radiated spectra, *Bull. Seismol. Soc. Am.* **73,** no. 6A, 1865–1894.

Boore, D. M., and W. B. Joyner (1997). Site amplifications for generic rock sites, *Bull. Seismol. Soc. Am.* **87,** no. 2, 327–341.

Chung, A. I., I. Henson, and R. M. Allen (2019). Optimizing earthquake early warning performance: Elarms-3, *Seismol. Res. Lett.* **90,** no. 2A, 727–743.

Day, S. M. (1982). Three-dimensional simulation of spontaneous rupture: The effect of nonuniform prestress, *Bull. Seismol. Soc. Am.* **72,** no. 6A, 1881–1902.

Dreger, D., E. Tinti, and A. Cirella (2007). Slip velocity function parameterization for broadband ground motion simulation, *Seismol. Res. Lett.* **78,** no. 2, 308.

Frankel, A. (2016). Modeling Strong-Motion Recordings of the 2010 M_w 8.8 Maule, Chile, earthquake with high stress-drop subevents and background slip, *Bull. Seismol. Soc. Am.* **107,** no. 1, 372–386.

Frankel, A., E. Wirth, N. Marafi, J. Vidale, and W. Stephenson (2018). Broadband synthetic seismograms for magnitude 9 earthquakes on the cascadia megathrust based on 3d simulations and stochastic synthetics, part 1: Methodology and overall results, *Bull. Seismol. Soc. Am.* **108,** no. 5A, 2347–2369.

Geuzaine, C., and J.-F. Remacle (2009). Gmsh: A 3-D finite element mesh generator with built-in pre- and post-processing facilities, *Int. J. Numer. Meth. Eng.* **79,** no. 11, 1309–1331.

Graves, R., and A. Pitarka (2014). Refinements to the Graves and Pitarka (2010) broadband ground-motion simulation method, *Seismol. Res. Lett.* **86,** no. 1, 75–80.

Graves, R. W., and A. Pitarka (2010). Broadband ground-motion simulation using a hybrid approach, *Bull. Seismol. Soc. Am.* **100,** no. 5A, 2095–2123.

Gregor, N. J., W. J. Silva, I. G. Wong, and R. R. Youngs (2002). Ground-motion attenuation relationships for Cascadia subduction zone megathrust earthquakes based on a stochastic finite-fault model, *Bull. Seismol. Soc. Am.* **92,** no. 5, 1923–1932.

Gusman, A. R., S. Murotani, K. Satake, M. Heidarzadeh, E. Gunawan, S. Watada, and B. Schurr (2015). Fault slip distribution of the 2014 Iquique, Chile, earthquake estimated from ocean-wide tsunami waveforms and GPS data, *Geophys. Res. Lett.* **42,** no. 4, 1053–1060.

Hayes, G. P. (2017). The finite, kinematic rupture properties of great-sized earthquakes since 1990, *Earth Planet. Sci. Lett.* **468,** 94–100.

Hayes, G. P., G. L. Moore, D. E. Portner, M. Hearne, H. Flamme, M. Furtney, and G. M. Smoczyk (2018). Slab2, a comprehensive subduction zone geometry model, *Science* **362,** no. 6410, 58–61.

Hoshiba, M., K. Iwakiri, N. Hayashimoto, T. Shimoyama, K. Hirano, Y. Yamada, Y. Ishigaki, and H. Kikuta (2011). Outline of the 2011 off the Pacific coast of Tohoku earthquake (M_w 9.0)—Earthquake early warning and observed seismic intensity, *Earth Planets Space* **63,** no. 7, 7.

Kamae, K., K. Irikura, and A. Pitarka (1998). A technique for simulating strong ground motion using hybrid Green's function, *Bull. Seismol. Soc. Am.* **88,** no. 2, 357–367.

Kuyuk, H. S., and R. M. Allen (2013). A global approach to provide magnitude estimates for earthquake early warning alerts, *Geophys. Res. Lett.* **40,** no. 24, 6329–6333.

Laske, G., G. Masters, Z. Ma, and M. Pasyanos (2013). Update on CRUST1. 0—A 1-degree global model of Earth's crust, in *Geophysical Research Abstract*, Vol. 15, EGU General Assembly Vienna, Austria, 2658 pp.

Lay, T., H. Yue, E. E. Brodsky, and C. An (2014). The 1 April 2014 Iquique, Chile, M_w 8.1 earthquake rupture sequence, *Geophys. Res. Lett.* **41,** no. 11, 3818–3825.

Leonard, M. (2010). Earthquake fault scaling: Self-Consistent relating of rupture length, width, average displacement, and moment release, *Bull. Seismol. Soc. Am.* **100,** no. 5A, 1971–1988.

LeVeque, R. J., K. Waagan, F. I. González, D. Rim, and G. Lin (2016). Generating random earthquake events for probabilistic tsunami hazard assessment, *Pure Appl. Geophys.* **173,** 3671–3692.

Liu, P., R. J. Archuleta, and S. H. Hartzell (2006). Prediction of broadband ground-motion time histories: Hybrid low/high-frequency method with correlated random source parameters, *Bull. Seismol. Soc. Am.* **96,** no. 6, 2118–2130.

Mai, P. M., and G. C. Beroza (2002). A spatial random field model to characterize complexity in earthquake slip, *J. Geophys. Res.* **107,** no. B11, 2309.

Mai, P. M., W. Imperatori, and K. B. Olsen (2010). Hybrid broadband ground-motion simulations: Combining long-period deterministic synthetics with high-frequency multiple *S*-to-*S* backscattering, *Bull. Seismol. Soc. Am.* **100,** no. 5A, 2124–2142.

Meier, M.-A., Y. Kodera, M. Böse, A. Chung, M. Hoshiba, E. Cochran, S. Minson, E. Hauksson, and T. Heaton (2020). How often can

earthquake early warning systems alert sites with high-intensity ground motion? *J. Geophys. Res.* **125,** no. 2, e2019JB017718.

Melgar, D., and G. P. Hayes (2017). Systematic Observations of the slip pulse properties of large earthquake ruptures, *Geophys. Res. Lett.* **44,** no. 19, 9691–9698.

Melgar, D., and G. P. Hayes (2019). The correlation lengths and hypocentral positions of great earthquakes, *Bull. Seismol. Soc. Am.* **109,** no. 6, 2582–2593.

Melgar, D., B. W. Crowell, J. Geng, R. M. Allen, Y. Bock, S. Riquelme, E. M. Hill, M. Protti, and A. Ganas (2015). Earthquake magnitude calculation without saturation from the scaling of peak ground displacement, *Geophys. Res. Lett.* **42,** no. 13, 5197–5205.

Melgar, D., R. J. LeVeque, D. S. Dreger, and R. M. Allen (2016). Kinematic rupture scenarios and synthetic displacement data: An example application to the Cascadia subduction zone, *J. Geophys. Res.* **121,** no. 9, 6658–6674.

Mena, B., P. M. Mai, K. B. Olsen, M. D. Purvance, and J. N. Brune (2010). Hybrid broadband ground-motion simulation using scattering Green's functions: Application to large-magnitude events, *Bull. Seismol. Soc. Am.* **100,** no. 5A, 2143–2162.

Minson, S. E., M.-A. Meier, A. S. Baltay, T. C. Hanks, and E. S. Cochran (2018). The limits of earthquake early warning: Timeliness of ground motion estimates, *Sci. Adv.* **4,** no. 3, eaaq0504.

Murray, J. R., B. W. Crowell, R. Grapenthin, K. Hodgkinson, J. O. Langbein, T. Melbourne, D. Melgar, S. E. Minson, and D. A. Schmidt (2018). Development of a geodetic component for the U.S. west coast earthquake early warning system, *Seismol. Res. Lett.* **89,** no. 6, 2322–2336.

Muto, M., and S. Krishnan (2011). Hope for the best, prepare for the worst: Response of tall steel buildings to the ShakeOut scenario earthquake, *Earthq. Spectra* **27,** no. 2, 375–398.

Pitarka, A., P. Somerville, Y. Fukushima, T. Uetake, and K. Irikura (2000). Simulation of near-fault strong-ground motion using hybrid Green's functions, *Bull. Seismol. Soc. Am.* **90,** no. 3, 566–586.

Rodgers, A. J., A. Pitarka, N. A. Petersson, B. Sjögreen, and D. B. McCallen (2018). Broadband (0–4 Hz) ground motions for a magnitude 7.0 Hayward fault earthquake with three-dimensional structure and topography, *Geophys. Res. Lett.* **45,** no. 2, 739–747.

Ruhl, C., D. Melgar, A. Chung, R. Grapenthin, and R. Allen (2019). Quantifying the value of real-time geodetic constraints for earthquake early warning using a global seismic and geodetic data set, *J. Geophys. Res.* **124,** no. 4, 3819–3837.

Ruhl, C. J., D. Melgar, R. Grapenthin, and R. M. Allen (2017). The value of real-time GNSS to earthquake early warning, *Geophys. Res. Lett.* **44,** no. 16, 8311–8319.

Schurr, B., G. Asch, S. Hainzl, J. Bedford, A. Hoechner, M. Palo, R. Wang, M. Moreno, M. Bartsch, Y. Zhang, *et al.* (2014). Gradual unlocking of plate boundary controlled initiation of the 2014 Iquique earthquake, *Nature* **512,** no. 7514, 299.

Takemura, S., T. Furumura, and T. Saito (2009). Distortion of the apparent *S*-wave radiation pattern in the high-frequency wavefield: Tottori-Ken Seibu, Japan, earthquake of 2000, *Geophys. J. Int.* **178,** no. 2, 950–961.

Trugman, D. T., M. T. Page, S. E. Minson, and E. S. Cochran (2019). Peak ground displacement saturates exactly when expected: Implications for earthquake early warning, *J. Geophys. Res.* **124,** no. 5, 4642–4653.

Wald, D. J. (2020). Practical limitations of earthquake early warning, *Earthq. Spectra*, 8755293020911388, 1–36.

Wells, D. L., and K. J. Coppersmith (1994). New empirical relationships among magnitude, rupture length, rupture width, rupture area, and surface displacement, *Bull. Seismol. Soc. Am.* **84,** no. 4, 974–1002.

Wirth, E. A., A. D. Frankel, N. Marafi, J. E. Vidale, and W. J. Stephenson (2018). Broadband synthetic seismograms for magnitude 9 earthquakes on the Cascadia megathrust based on 3d simulations and stochastic synthetics, part 2: Rupture parameters and variability, *Bull. Seismol. Soc. Am.* **108,** no. 5A, 2370–2388.

Ye, L., T. Lay, H. Kanamori, and L. Rivera (2016). Rupture characteristics of major and great ($M_w \geq 7.0$) megathrust earthquakes from 1990 to 2015: 1. Source parameter scaling relationships, *J. Geophys. Res.* **121,** no. 2, 826–844.

Zhu, L., and L. A. Rivera (2002). A note on the dynamic and static displacements from a point source in multilayered media, *Geophys. J. Int.* **148,** no. 3, 619–627.

Manuscript received 28 January 2020
Published online 14 July 2020